Chaos, Solitons and Fractals 163 (2022) 112518

Contents lists available at ScienceDirect

Chaos, Solitons and Fractals

journal homepage: www.elsevier.com/locate/chaos

Vegetation covers phase separation in inhomogeneous environments

D. Pinto-Ramos [a,*,1], S. Echeverría-Alar [a,1], M.G. Clerc [a,1], M. Tlidi [b,1]

[a] Departamento de Física and Millennium Institute for Research in Optics, Facultad de Ciencias Físicas y Matemáticas, Universidad de Chile, Casilla 487-3, Santiago, Chile

[b] Faculté des Sciences, Université libre de Bruxelles (ULB), CP. 231, 1050 Brussels, Belgium

ABSTRACT

Vegetation patterns in arid and semi-arid ecosystems as a self-organized response to resource scarcity is a well-documented issue. Their formation is often attributed to the symmetry-breaking type of instability. In this contribution, we focus on a regime far from any symmetry-breaking instability and consider a bistable regime involving uniformly vegetated covers and a bare state. We show that vegetation populations exhibit non-random two-phase structures where high biomass density regions are separated by sparsely covered areas or even bare soil. These structures are referred to as phase separation vegetation covers. We provide observations of this phenomenon in Gabon, Angola, Argentina, and Mexico. The inhomogeneities in environmental conditions are crucial to explain the origin of phase separation vegetation covers. We derive a simple equation from ecologically relevant models to explain various field observations. The bifurcation diagrams obtained from this model allow us to prove that inhomogeneity in the aridity parameter is a source of resilience for vegetation covers, avoiding collapsing towards a bare state. We characterize the natural observations and the equilibria from the model by using Fourier transform technique, spatial autocorrelation analysis, and size distribution of patches analysis.

1. Introduction

The fragmentation of landscapes and loss of biological production in drylands, which leads to desertification as a result of climate change and longer drought periods, is one of the world's most pressing environmental challenges. This fragmentation is typically accompanied by a non-equilibrium symmetry breaking instability, even when the topology of the landscapes is flat [1,2]. The patterns that emerge from the symmetry-breaking instability is generically called vegetation patterns. The 'tiger bush' is a well-known example that was first seen in the early 1940s thanks to the development of aerial photography [3]. Since this discovery, several modeling approaches have been proposed to explain the origin of these patterns, ranging from cellular-automata models [4], integrodifferential equations [1], reaction–diffusion equations [5–8], to spatially stochastic models [9,10]. The later approach focuses on how environmental randomness can be used to create symmetry-breaking transitions that lead to the formation of vegetation patterns. Besides tiger bush other spatially periodic vegetation patterns have been reported such as hexagons [1,2,11,12], and labyrinths [2,12].

Vegetation patterns are not always periodic. They can be localized in space [13–17], found close to the symmetry-breaking instability. In [18,19], it is established how two well separated isolated patches interact in one- and two-dimensions. As one moves out from the patch center, the patch tail monotonically decays, whereas localized gaps have a damped oscillatory tail. Depending on how far apart the gaps are, the interaction can be either attractive or repulsive [20]. Localized patches may exhibit a curvature instability that causes the self-replication phenomenon [21,22] or the emergence of arcs and spirals [23].

Nonperiodic vegetation patterns in a regime far from any symmetry-breaking instability can be observed in nature. These structures emerge spontaneously from random perturbations of the unstable homogeneous steady state that separates the two stable states forming a bistable system. This phenomenon is referred as phase separation. Growth of spatial domains of different phases whose dynamics is governed by power law in systems with conserved and nonconserved order parameters is a well documented issue [24–26]. This phenomenon has been studied in a variety of out-of-equilibrium systems, including polymer chemistry [27,28], material science [29], optical systems [30–33] and cell biology [34]. However, the topic of phase separation in ecosystems caused by environmental inhomogeneity has received little attention.

Examples of phase separation in ecosystems are shown in Fig. 1. These are satellite photos, retrieved from Google Earth software, of vegetation coverage in different regions. Near the African coast, the landscapes of Gabon (see Fig. 1a) and Angola (see Fig. 1b) show distinct patches of bare soil and planted areas of various sizes and forms. Scattered vegetated and non-vegetated areas are seen in the hilly regions of Argentina (see Fig. 1c) and Mexico (see Fig. 1d). It is seen that the vegetation distribution in all these places is inhomogeneous. Modeling

* Corresponding author.
E-mail address: david.pinto@ug.uchile.cl (D. Pinto-Ramos).

[1] David Pinto-Ramos, Sebastián Echeverría-Alar, Marcel G. Clerc, and Mustapha Tlidi contributed equally to the production of this work.

https://doi.org/10.1016/j.chaos.2022.112518
Received 30 June 2022; Received in revised form 27 July 2022; Accepted 28 July 2022
Available online 17 August 2022

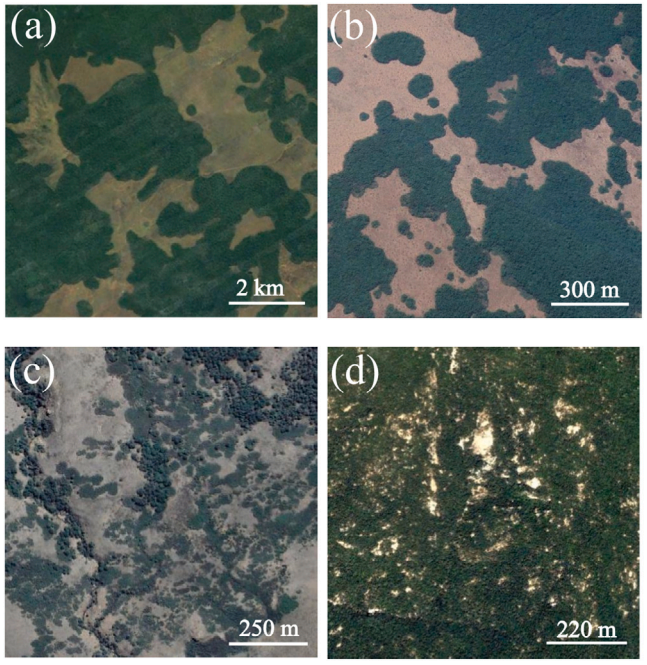

Fig. 1. Vegetation pattern phase separation. Top views of (a) Gabon, Africa (2° 44' 08.42" S, 10° 12' 28.37" E), (b) Angola, Africa (6° 19' 39.10" S, 12° 35' 25.98" E), (c) Argentina, South America (40° 58' 17.21" S, 71°16' 03.76" O), and (d) Mexico, North America (29° 04' 25.99" N, 110° 11' 19.27" O).

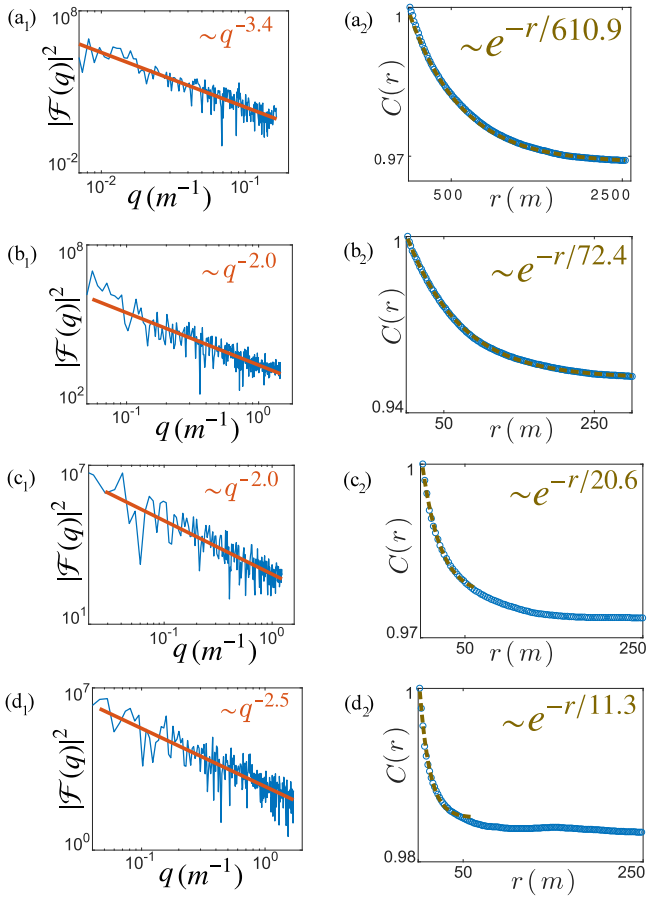

Fig. 2. Fourier spectra and spatial autocorrelations. The blue dots and the blue lines represent the real data from the vegetation images of Fig. 1. (a_1, b_1, c_1, and d_1) correspond to the Fourier spectrum of Gabon, Angola, Argentina, and Mexico vegetation patterns, respectively. The red line in the Fourier space illustrates the power-law behavior of the tail in the radial direction q. The exponents range from 2.0 to 3.4. The R^2 values of the linear fittings are (a_1) 0.79, (b_1) 0.77, (c_1) 0.69, and (d_1) 0.70, respectively. (a_2, b_2, c_2, and d_2) are autocorrelations corresponding to Gabon, Angola, Argentina, and Mexico vegetation patterns, respectively. The characteristic correlation lengths l are (a_2) $l = 610.9$ m, (b_2) $l = 20.6$ m, (c_2) $l = 11.3$ m, and (d_2) $l = 72.4$ m. They are obtained by fitting the exponential law $Be^{-r/l}$ to the real data, where B is a positive constant. The R^2 value of all the exponential fittings is 0.99. (For interpretation of the references to color in this figure legend, the reader is referred to the web version of this article.)

approaches in vegetation ecosystems do not exhibit heterogeneous non-periodic self-organization as equilibrium. The spatial characterization of such vegetation states and the transitions between them have not been explored.

We propose a unified description for non-homogeneous and non-periodic vegetation covers, vegetation pattern phase separation. We show that the inhomogeneous vegetation covers are equilibrium states of the ecosystem under inhomogeneous environment. We demonstrate how the inclusion of inhomogeneities in the parameters plays a crucial part in explaining the wide range of distinct observed equilibria. We observe that the vegetation spatial organization is characterized by a power-law distribution in Fourier space and an exponential decay in the spatial correlation. Finally, a power law for the early temporal evolution of the total biomass is numerically inferred .

Following an introduction, Section 2 shows the characterization of the spatial self-organization of the satellite images in Fig. 1. In Section 3, we present a straightforward Fisher–Kolmogorov–Petrovskii–Piskunov (FKPP) type model with inhomogeneous environmental conditions and explore the dynamics of phase separation vegetation covers. The study of equilibria and the coarsening dynamics of homogeneous states are discussed in Sections 4 and 5, respectively. In Section 5.2, we examine how the coarsening dynamics are impacted by an inhomogeneous environment by avoiding collapse to the bare state. The paper is concluded in Section 6. A detailed derivation of the FKPP equation from the generic interaction redistribution model and the reaction–diffusion water and biomass model is included in the Appendix section.

2. Spatial characterization of field observations

To characterize vegetation phase separation patterns shown in Fig. 1, we evaluate their Fourier spectrum and their spatial autocorrelation. The results are shown in Fig. 2, where the Fourier spectrum $|F(q)|^2$, as a function of the radial wavevector q, is depicted in Fig. 2(a_1, b_1, c_1, d_1). All satellite images taken from Gabon, Angola, Argentina, and Mexico unexpectedly possess a power-law decaying tail connecting a range of spatial scales in the wavevector space. In this figure, the linear fitting is indicated by red line. At the very least, this eliminates the possibility of a wavelength selection process leading to the formation of periodic vegetation patterns. Besides, each vegetation photograph of Fig. 1 is accompanied by spatial autocorrelation function $C(r)$ as a function of a distance r [see Fig. 2(a_2)]. The vegetation structures have a spatial autocorrelation characterized by an exponential decay behavior until an asymptotic value is reached. Up until great distances, Gabon shown in Fig. 2(a_2) and Angola shown in Fig. 2 (b_2) exhibit an exponential behavior. At small distances, the exponential decay is truncated in Argentina and Mexico as shown in Fig. 2(c_2) and Fig. 2(d_2), respectively. The exponential decay is represented by fitting curves of the form $\sim e^{-r/l}$ of the autocorrelation data [see brown dashed lines in panels of Fig. 2(a_2, b_2, c_2, d_2)]. The correlation length is denoted by l, which describes the local vegetation pattern phase-separation of a well defined mean patch size. In fact, a closer look at the vegetation covers in Fig. 1 reveals nonperiodic behavior, leaving aside the explanation of spontaneous symmetry-breaking mechanisms.

The Fourier spectra together with spatial autocorrelations indicated that the vegetation patterns observed in Africa and America reported in

Fig. 1 do not emerge spontaneously from symmetry-breaking instability but rather from phase separation mechanism. Independent of the region of the planet, and type of soil and vegetation (bushes, patches, shrubs, trees), we observe a power-law in Fourier space and an exponential decay of the autocorrelation function. In the next sections, we introduce a model and provide an explanation to the field observations.

3. Phase separation dynamics for biomass

We adopt a continuous time and space description of the biomass density $b(x, y, t)$ at space coordinates $\mathbf{r} = (x, y)$ and time t. Theory of vegetation patterns based on the non-local FKPP equation has been reported in [35–37]. In this contribution, we consider the paradigmatic local FKPP [38,39] model equation describing the population dynamics of individuals with the inclusion of small inhomogeneities in the growth parameter

$$\partial_t b = -\left(\eta + \sqrt{\Gamma}\xi(\mathbf{r})\right) b + \kappa b^2 - b^3 + D\nabla^2 b. \tag{1}$$

This simple model is derived from the nonlocal FKPP equation, and from reaction–diffusion water biomass model (see the Appendix). The parameter η measures the linear growth ($\eta < 0$) or decay ($\eta > 0$) of vegetation population. η increases as the aridity of the environment increases; κ measures the net effect of facilitative versus competitive interactions, and b^3 is the nonlinear saturation. The last term describes diffusion with coefficient D and $\nabla^2 = \partial_{xx} + \partial_{yy}$ is the bidimensional laplacian operator. The degree of aridity described by the parameter η of an environment is related with on-site evapotranspiration process [40]. A spatial distribution of this process can arise naturally due to different type of soil, diverse plant groups, and topographic variations [41]. The function $\xi(\mathbf{r})$ models these environmental inhomogeneities and Γ measures the intensity of them.

Let us briefly recall that Eq. (1) can be stated in gradient form

$$\partial_t b = -\frac{\delta F}{\delta b},$$
$$F \equiv \int d\mathbf{r}\left(\eta(\mathbf{r})\frac{b^2}{2} - \kappa\frac{b^3}{3} + \frac{b^4}{4} + \frac{D}{2}(\nabla b)^2\right), \tag{2}$$

where $\eta(\mathbf{r}) = \eta + \sqrt{\Gamma}\xi(\mathbf{r})$. Then, it is well-known that the system Eq. (1) will reach an equilibrium minimizing the potential F.

In what follows, we focus on the effects of independent inhomogeneities in space. In this case, the function $\xi(\mathbf{r})$ is generated by a delta-correlated gaussian random process of zero mean. In the absence of inhomogeneities, i.e., $\Gamma = 0$, the model for vegetation Eq. (1) was derived from ecologically relevant models (see the Appendix). It has also been derived from a variety of physical systems, including liquid crystals [42], flame combustion [43], fiber Kerr resonators [44], passive Kerr cavity [45], and electrical circuits [46], to mention a few.

Eq. (1) for $\Gamma = 0$ supports domain walls [47] (or bistable fronts) separating the two stable equilibrium states $b_{h1} = (\kappa + \sqrt{\kappa^2 - 4\eta})/2$ and $b_{h2} = 0$. One important aspect of equilibria, is that for positive values of κ there exist a tipping – or saddle node – point at $b_s = \kappa/2$ and $\eta_s = \kappa^2/4$. As one crosses the critical aridity $\eta = \eta_s$, this bifurcation, which is defined by the annihilation of two equilibria, causes dramatic changes in the system [48], well documented as catastrophic shift in ecology.

The dynamics of Eq. (1) in the simple case of homogeneous environmental conditions, is characterized by front propagation. Straightforward calculations lead to a propagation speed of the fronts proportional to the difference of energy of the homogeneous states. Neglecting the curvature effects for the domain propagation, the speed of walls reads (see the textbook [47] and reference therein)

$$v_{walls}(b_{h1} \to b_{h2}) \equiv v_0 \propto F(b_{h2}) - F(b_{h1}), \tag{3}$$
$$F(b) \equiv \eta\frac{b^2}{2} - \kappa\frac{b^3}{3} + \frac{b^4}{4}. \tag{4}$$

In homogeneous environmental conditions where η is a constant, the dynamics leads to either a uniform vegetated cover or a state totally devoid of vegetation. This approximation cannot explain the wide range of vegetation patterns depicted in Fig. 1. It is then necessary, to include inhomogeneities in the environmental conditions, such as the aridity, which will explain the field observation as we will see in the next section.

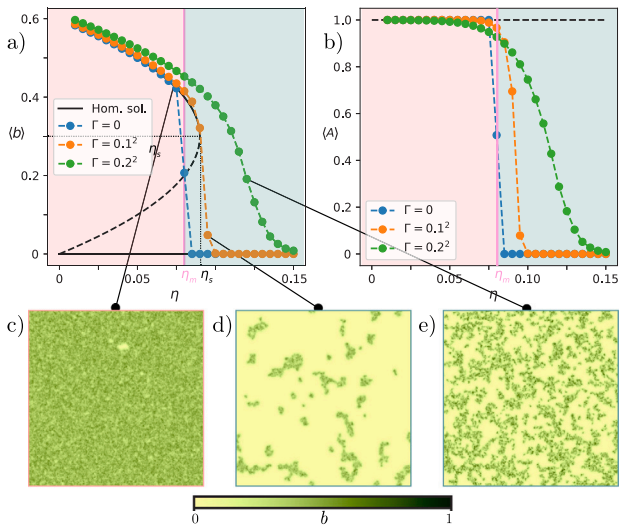

Fig. 3. The bifurcation diagram of Eq. (1) for parameters $\kappa = 0.6$ and $D = 0.1$, showing the different behaviors for different Γ values. (a) Bifurcation diagram for the averaged biomass $\langle b\rangle$. (b) Bifurcation diagram for the area fraction $\langle A\rangle$. (c), (d) and (e) show examples of the different equilibria exhibited in the bifurcation diagram. (For interpretation of the references to color in this figure legend, the reader is referred to the web version of this article.)

4. Equilibrium states analysis

In this section, we discuss equilibria of Eq. (1) first in the homogeneous parameter $\Gamma = 0$ case, and then when $\Gamma \neq 0$, considering both delta-correlated and spatial correlated inhomogeneities.

4.1. Homogeneous case $\Gamma = 0$

Starting from random initial conditions $b_i(\mathbf{r}, 0)$ around the unstable vegetated state, one can introduce the averaged biomass $\langle b\rangle \equiv \sum_{i=1}^{N}\int d\mathbf{r} b_i(\mathbf{r}, T)/NL^2$, where N is the number of realizations and T is the time to reach equilibrium. $\langle b\rangle$ exhibits an abrupt change when increasing the aridity parameter η as shown by the blue dotted curve in Fig. 3(a). There exist a single point called the Maxwell point and denoted by $\eta = \eta_m$, where front solutions of Eq. (1) are stationary, i.e., when the two stable homogeneous steady states have the same energy. For $\eta < \eta_m$, b_{h1} has the lowest free energy density, whereas for $\eta > \eta_m$, $b_{h2} = 0$ is the preferred state. Figs. 3(b) illustrates the bifurcation diagram for the mean biomass $\langle b\rangle$ and the biomass area fraction $\langle A\rangle \equiv \sum_{i=1}^{N}\int d\mathbf{r} A_i(\mathbf{r}, T)/NL^2$, respectively. The latter is defined using the binarized biomass field A_i for different initial conditions b_i as

$$A_i(\mathbf{r}, T) \equiv \begin{cases} 1 & \text{if } b_i(\mathbf{r}, T) \geq b_s = \kappa/2, \\ 0 & \text{if } b_i(\mathbf{r}, T) < b_s = \kappa/2. \end{cases} \tag{5}$$

The biomass area fraction corresponding to the case $\Gamma = 0$ is indicated by the blue dotted curve in Fig. 3(b). Without inhomogeneities, numerical simulations of Eq. (1) for a long time evolution, reach either a uniform cover state or a state totally devoid of vegetation. These equilibrium biomass covers correspond to an area fraction one or zero in Fig. 3(b), respectively. Therefore, vegetation patterns and phase separation vegetation covers are excluded in this case.

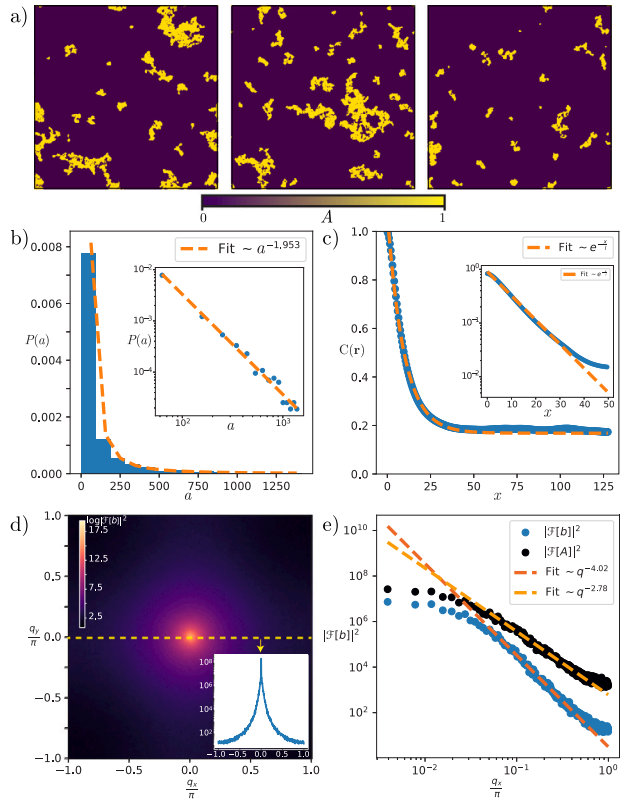

Fig. 4. Statistical analysis of a low area fraction equilibrium for parameters $\kappa = 0.6$, $D = 0.1$, $\eta = 0.95$, and $\Gamma = 0.01$. (a) Examples of equilibrium A fields. (b) Probability density of patch area $P(a)$ with a power law fit and its logarithmic scale graph in the inset. (c) Autocorrelation function of the b field, showing an exponential fit and a semi logarithmic scale graph in the inset. (d) Averaged absolute value of the Fourier transform of b in semi logarithmic scale (for contrast purposes). (e) Logarithmic scale graph for the tail of the Fourier transform with power law fits for the A and b fields. (For interpretation of the references to color in this figure legend, the reader is referred to the web version of this article.)

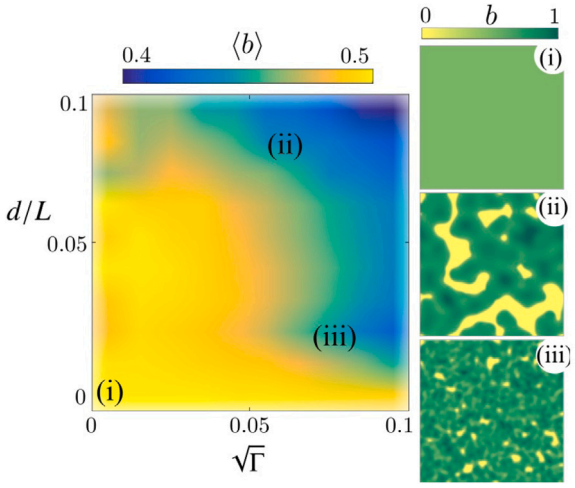

Fig. 5. Steady state averaged biomass $\langle b \rangle$ from Eq. (1) with spatially correlated inhomogeneities. The surface-plot show the average biomass $\langle b \rangle$ for different values of the intensity $\sqrt{\Gamma}$ and the degree of correlation d/L of the inhomogeneities. d is the correlation length of the $\xi(\mathbf{r})$ function, obtained by fitting an exponential law to the autocorrelation $C(\mathbf{r})$ of $\xi(\mathbf{r})$, and L is the size of the simulation box. All the correlated $\xi(\mathbf{r})$ were created with the reaction–diffusion process ($\epsilon = 0.1$). (i) $d/L = 0$ and $\sqrt{\Gamma} = 0$, (ii) $d/L = 0.03$ and $\sqrt{\Gamma} = 0.08$, and (iii) $d/L = 0.08$ and $\sqrt{\Gamma} = 0.07$ correspond to different equilibria obtained in Eq. (1). The biomass b is normalized to 1 in the three insets. (For interpretation of the references to color in this figure legend, the reader is referred to the web version of this article.)

4.2. Inhomogeneous $\Gamma \neq 0$ and non-correlated $\xi(\mathbf{r})$ case

When the aridity parameter is inhomogeneous $\Gamma \neq 0$, numerical simulations of Eq. (1), using different random initial conditions and different realizations of $\xi(\mathbf{r})$, show there is no abrupt change in the mean biomass for large enough Γ. Fig. 3(a) show this smooth transition (see orange and green curves). In this case, the transition is rather continuous avoiding a catastrophic shift in the ecosystem.

Contrarily to the homogeneous case, the system can reach phase separation vegetation covers as shown in Figs. 3(c, d, e). Now, the system is characterized by the coexistence of disordered patches of vegetation and bare soil. According to the bifurcation diagram in Fig. 3(b), equilibrium biomass covers can have an area fraction other than zero or one. Note that states with low area fraction ($\langle A \rangle \ll 1$) are found above the Maxwell point ($\eta > \eta_m$) (cf. Figs. 3(d) and 3(e)). However, states with high area fraction ($1 - \langle A \rangle \ll 1$) are only found below the Maxwell point ($\eta < \eta_m$), as shown in Fig. 3(c).

Inhomogeneities can prevent plants from collapsing to bare ground. It is important to notice that even for entirely uncorrelated inhomogeneities, one can recognize the spatial structures seen in vegetation (see Fig. 1), and predicted by the FKPP Eq. (1). One can identify the location and size of patches by using ImageJ software [49], which has been applied to the field A. Fig. 4(a) shows examples of the field A for different realizations of the numerical simulations. It is interesting to note that the probability distribution of patch sizes $P(a)$, where a is the area of a biomass patch, follows a power law as shown in Fig. 4(b). This $P(a)$ behavior is in line with some measurement for small patch sizes that have been documented in the literature [50]. In addition, as shown in Figs. 4(d) and 4(e), the tails of the Fourier transform of the $b_i(\mathbf{r}, T)$ and $A_i(\mathbf{r}, T)$ fields both follow a power law, typical of complex systems [51,52]. This Fourier space structure translates into a well-defined correlation function with an exponential decay for equilibrium states produced by the model Eq. (1), as shown in Fig. 4(c). We compare the outcomes of numerical simulations of the model equation with the satellite photos provided in Fig. 1 thanks to these straightforward analysis tools.

4.3. Inhomogeneous $\Gamma \neq 0$ and correlated $\xi(\mathbf{r})$ case

In what follows, we address the problem of considering the effects of inhomogeneities that are spatially correlated. To have spatially correlated inhomogeneities, let us consider an initial delta correlated function $\xi(\mathbf{r})$, to go through a simple reaction–diffusion process

$$\partial_s \xi(\mathbf{r}) = -\epsilon \xi(\mathbf{r}) + \nabla^2 \xi(\mathbf{r}), \tag{6}$$

where ϵ is a positive relaxational constant, and s parametrizes the evolution of $\xi(\mathbf{r})$. We extract different temporal stages of this evolution. In this way, we obtain inhomogeneity functions with a degree of spatial correlation, which is characterized by the dimensionless parameter d/L. d is the correlation length and L is the system size. After, we normalize the correlated functions $\xi(\mathbf{r}, s)$ between $[-1, 1]$ in order to control the inhomogeneities in Eq. (1) with the inhomogeneity level intensity Γ. Fig. 5 shows the averaged biomass $\langle b \rangle$ from Eq. (1) for different values of the inhomogeneity intensities Γ and correlation lengths d of the inhomogeneities $\xi(\mathbf{r})$. When increasing d, $\langle b \rangle$ decreases (see insets (ii) and (iii) in Fig. 5) in comparison to the homogeneous case shown in the inset (i) of Fig. 5. This is related to the coherent patches of bare soil that can coexist with the vegetated state thanks to incorporating a correlated inhomogeneity function $\xi(\mathbf{r})$. The addition of the spatial correlation can capture more smooth vegetation distributions, which are comparable to the satellite images of Gabon and Angola (cf. Figs. 1(a) and 1(b), respectively).

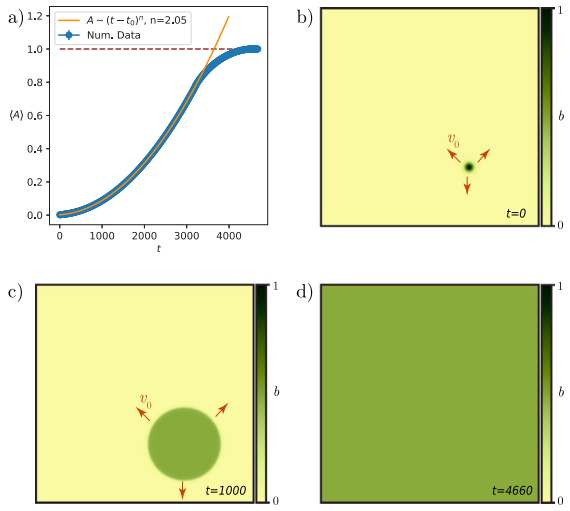

Fig. 6. Biomass propagation in homogeneous landscape. (a) The blue dots are the temporal evolution of the area cover for numerical simulations of Eq. (1), with parameters $\kappa = 0.6$, $D = 0.1$, $\eta = 0.02$, and $\Gamma = 0$. The orange indicates the theoretical prediction from Eq. (9). (b), (c), and (d) are different stages of propagation, showing that homogeneous conditions favor circular patches and full cover at equilibrium. (For interpretation of the references to color in this figure legend, the reader is referred to the web version of this article.)

5. Coarsening dynamics

In the last section, we analyze the early temporal evolution of the biomass density field $b(x, y, t)$ that leads to the equilibrium states discussed previously.

5.1. Coarsening in homogeneous environment

From the front or wall speed Eq. (3), one can infer the temporal evolution for the total cover of the biomass b as depicted in Fig. 6(a). For this, consider that a localized portion of vegetation (patch) is placed on bare ground $b = 0$, as shown in Fig. 6(b). Then, the interface propagates, as seen in Figs. 6(c) and 6(d), with an approximated speed of v_0 (see Section 3 and Eq. (3)). Thus, the characteristic size of the patch increases linearly with time t as

$$\langle L_{patch} \rangle \sim v_0 t. \tag{7}$$

Then, it is straightforward to introduce the total biomass and the area of a patch A_{patch} by

$$b_{total} \sim b_{h1} \langle L_{patch} \rangle^2 \equiv b_{h1} \langle A_{patch} \rangle. \tag{8}$$

From this, one can easily see that

$$\langle A_{patch} \rangle \sim t^n, \tag{9}$$

with $n = 2$. The previous expression is valid for a single patch in space neglecting curvature effects. Otherwise, front interactions and curvature effects alter the simple dynamics of the front. Fig. 6 (a) shows perfect agreement with this simple theory by fitting Eq. (9) to the numerical data.

More interesting is the natural nucleation of multiple patches after an initial perturbation. Initializing the system with random initial conditions, small deviations from the critical exponent $n = 2$ are expected due to multiple patch nucleation, as seen in Figs. 7(a) and (b) for early times. Figs. 7(c) to 7(f) show the temporal evolution of the nucleation of patches. Note that as one gets closer to the Maxwell point, the interaction between walls becomes stronger, and we expect larger deviations from the naive exponent $n = 2$. Unexpectedly, a crossover between exponents $n = 2$ and $n = 3$ is observed for low area fractions $\langle A \rangle$ with the former dominating the early time dynamics.

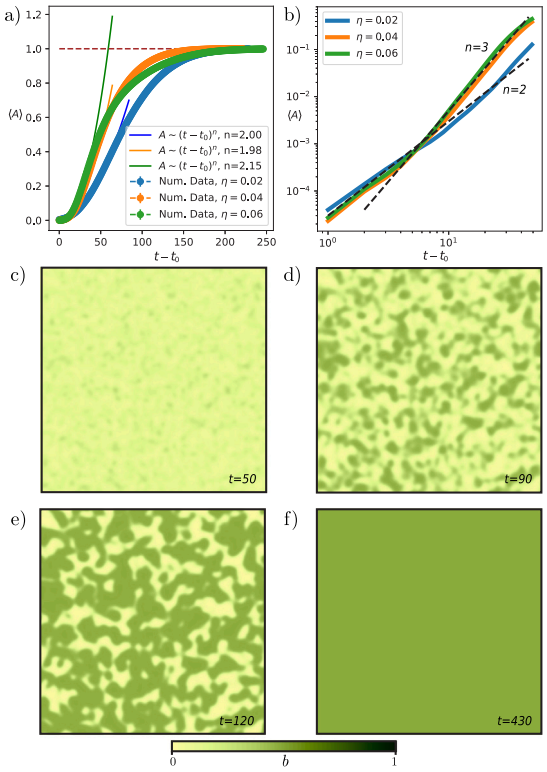

Fig. 7. Temporal dynamics of multiple patch growth in homogeneous landscape. (a) and (b) exhibit the temporal dynamics following power laws in time for the vegetation area cover, calculated from numerical simulation data of Eq. (1) with parameters $\kappa = 0.6$, $D = 0.1$, and $\Gamma = 0$. (c), (d), (e) and (f) show different stages of temporal evolution with coarsening dynamics. (For interpretation of the references to color in this figure legend, the reader is referred to the web version of this article.)

5.2. Coarsening in an inhomogeneous environment

In the case $\Gamma \neq 0$, fronts can suffer from a pinning phenomenon [53], explaining the amorphous shapes we can observe as equilibrium states. Pinning phenomenon has been studied in several fields of physics, appearing naturally in discrete systems such as crystal lattices [54], and pattern forming systems [55]. Spatially modulated parameters could also induce pinning phenomenon as observed in liquid crystal devices [56] or granular media [57].

For the temporal dynamics, fronts will be highly coupled to the external inhomogeneities imposed, putting in doubt the validity of Eq. (7). Surprisingly, coarsening dynamics for low area fractions were observed, although with a different exponent n compared with the homogeneous case, as seen in Fig. 8.

One can see that inhomogeneities increase the characteristic exponent for the area cover growth, from $n = 2$ to $n = 4$. Indeed, it is observed that inhomogeneities dramatically accelerate evolution towards the equilibrium state, reaching an almost full cover approximately fifty times faster compared to the homogeneous case $\Gamma = 0$ case.

6. Conclusions

We have reported satellite photos showing phase separation vegetation covers, obtained from Google Earth software in different landscapes of Africa and America. We have characterized vegetation phase separation patterns by establishing their Fourier spectra and spatial autocorrelations. We have demonstrated that these patterns, independent of the plant involved and the type of soil in which they are observed, exhibit a generic power-law in Fourier space and exponential decay of the autocorrelation function. Thanks to this investigation, we were able

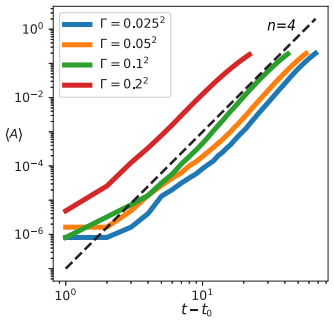

Fig. 8. Effect of inhomogeneities on early temporal evolution. The area cover of vegetation shows a different exponent for its temporal dynamics, from numerical simulations of Eq. (1) with delta correlated $\xi(\mathbf{r})$, parameters $\kappa = 0.6$, $D = 0.1$, $\eta = 0.02$. (For interpretation of the references to color in this figure legend, the reader is referred to the web version of this article.)

to rule out the symmetry-breaking mechanism caused by the formation of periodic vegetation patterns.

We have derived a simple equation, the local FKPP, as a paradigm for the studying of population dynamics, from the generic interaction redistribution model, and the reaction–diffusion water and biomass model. We have demonstrated that environmental inhomogeneities are necessary to account for the phase separation patterns observed in vegetation. Numerical simulations for a long time evolution showed that the model Eq. (1) without inhomogeneities cannot support phase separation vegetation covers.

Simple static indicators such as patch size distributions, spatial Fourier transform analysis, and correlation functions analysis reveal the presence of inhomogeneities. Additionally, we propose dynamical indicators given by the coarsening power-law exponents for the early time evolution of vegetation covers.

More importantly, inhomogeneities are shown to be a source of resilience for vegetation covers. We demonstrated that enough inhomogeneities allowed to avoid collapsing towards a bare state, shedding light on mechanisms to preserve arid ecosystems from the global warming process and long drought periods.

Declaration of competing interest

The authors declare that they have no known competing financial interests or personal relationships that could have appeared to influence the work reported in this paper.

Data availability

Data will be made available on request.

Acknowledgments

D.P.-R. acknowledges the financial support of ANID National Ph.D. scholarship, Chile 2020-21201484. M.G.C. acknowledges the financial support of ANID-Millennium Science Initiative Program-ICN17_012 (MIRO), Chile and FONDECYT, Chile project 1210353. S.E.-A. acknowledges the financial support of ANID National Ph.D. scholarship, Chile 2020-21201376. M.T. is a Research Director at Fonds de la Recherche Scientifique FNRS.

Appendix

A.1. Nonlocal FKPp model

The nonlocal FKPP model for vegetation population reads [20,35]

$$\partial_t b = b(1-b)m_f(\mathbf{r}) - \mu b m_c(\mathbf{r}) + D m_D(\mathbf{r}), \tag{10}$$

$$m_{f,c} = \exp(\chi_{f,c} \int d\mathbf{r}' \phi_{f,c}(\mathbf{r}') b(\mathbf{r}+\mathbf{r}')), \tag{11}$$

$$m_D = \int d\mathbf{r}' \phi_D(\mathbf{r}') \left[b(\mathbf{r}+\mathbf{r}') - b(\mathbf{r}) \right], \tag{12}$$

where b corresponds to the biomass density field, following a logistic growth depending on the neighboring biomass with m_f. Mortality has a base rate μ enhanced by competition feedback through m_c. The seed dispersion is described by the last term in the rhs of Eq. (10). The nonlocal terms Eqs. (11) and (12) correspond to a weighted sum of the biomass with kernels $\phi_{f,c,D}(\mathbf{r}')$. These kernels are decaying functions of the distance between interacting plants, and are assumed to be radially symmetric. They model facilitative (f), competitive (c), and seed dispersion (D) processes. The strength of the competitive and facilitative interactions are χ_f and χ_c, respectively. Whereas D is the intensity of seed dispersion.

We perform a weak nonlinear analysis in Eq. (10). First, note the critical parameter $\mu = \mu_c = 1$ at which the bare soil state $b = 0$ changes its stability. The curve defining the non-trivial homogeneous equilibria is $0 = (1-b)\exp(\chi_f b) - \mu \exp(\chi_c b)$, and has two positive solutions for $\chi_f - \chi_c \geq 1$. These solutions collapse to the $b = 0$ state at $\chi_f - \chi_c = 1$ and $\mu = \mu_c$. Let us explore the vicinity of the onset of bistability by introducing a small parameter ϵ ($\epsilon \ll 1$) that describes the distance from criticality as

$$\mu = \mu_c + \epsilon^2 \eta, \tag{13}$$

$$\chi_f - \chi_c = 1 + \epsilon\kappa. \tag{14}$$

A linear analysis of Eq. (10) around $b = 0$ with finite wavevector perturbation $b = A\exp(i\mathbf{q}\cdot\mathbf{r} + \lambda t)$ leads to the characteristic equation $\lambda(\mathbf{q}) = 1 - \mu + D(\hat{\phi_D}(\mathbf{q}) - 1)$, where $\hat{\phi_D}(\mathbf{q})$ is the Fourier transform of $\phi_D(\mathbf{r})$. Remembering that the kernels are normalized, it follows that $\hat{\phi}_{f,c,D}(\mathbf{q} = 0) = 1$. Moreover, as the kernels are radially symmetric the expansion for large wavelength perturbation reads $\hat{\phi_D}(\mathbf{q}) \approx 1 + \partial_{q_x q_x}\hat{\phi_D}(\mathbf{0})\mathbf{q}^2/2 + \cdots$, having at dominant order the band of unstable modes $\Delta q^2 = (\mu - 1)/(D\partial_{q_x q_x}\hat{\phi_D}(\mathbf{0})/2) \sim \epsilon^2$. Then, we propose the ansatz

$$b = \epsilon A(T = \epsilon^2 t, \mathbf{R} = \epsilon\mathbf{r}) + \epsilon^2 W^{[2]} + \epsilon^3 W^{[3]} + \cdots, \tag{15}$$

where $W^{[n]}$ correspond to nonlinear corrections of order ϵ^n. Additionally, we expand the integral terms, provided that the kernels in Eqs. (11) and (12) decay faster than an exponential, as

$$\int d\mathbf{r}' \phi_{f,c,D}(\mathbf{r}') b(\mathbf{r}+\mathbf{r}') \approx b(\mathbf{r}) + \frac{\nabla^2 b}{4} \int d\mathbf{r}' \phi_{f,c,D}(\mathbf{r}') \mathbf{r}'^2 + \cdots$$

By replacing this expansion and Eqs. (13), (14), (15) in Eq. (10) a hierarchy of equations at different orders in ϵ are found. Orders ϵ and ϵ^2 satisfy automatically the solvability condition, and at ϵ^3 order we get the equation

$$\partial_T A = -\eta A + \kappa A^2 - A^3/2 + D_e \nabla^2 A, \tag{16}$$

where

$$D_e = \frac{D}{4} \int d\mathbf{r}' \phi_D(\mathbf{r}') \mathbf{r}'^2. \tag{17}$$

In this way, with a renaming and scaling of variables and parameters in Eq. (16), we recover the local FKPP Eq. (1).

A.2. Water and biomass model

Another popular approach to explain the vegetation pattern formation proposed in the literature is based on water transport [5–8]. When biomass and water interact, vegetation ecosystems can be modeled by a pair of coupled reaction–diffusion equations. A general approach when considering sloped territory was provided in [5]. A model considering the possible bistability between bare soil and populated state reads [58]

$$\begin{aligned}\partial_t b &= b(1-b)w(1+\gamma b)^2 - \mu b + D\nabla^2 b,\\ \partial_t w &= p - w - \sigma b w(1+\gamma b)^2 + \nabla^2 w.\end{aligned} \tag{18}$$

Where b and w correspond to the biomass and ground water density fields, respectively. γ characterizes the increase of biomass production with water consumption. The parameter μ represents the mortality rate and D accounts for the dispersal by seeds. The parameter p models the mean water input to the system, and σ weights the water lost by consumption of the biomass.

We can derive a normal form equation for long wavelength perturbations near the onset of bistability. Let us consider the linear dynamics around the bare soil state as $(b,w) = (0,p) + \delta A\vec{v}\exp(i\mathbf{q}\cdot\mathbf{r} + \lambda t)$, with $\delta A \ll 0$, the jacobian reads

$$J = \begin{pmatrix} p-\mu-Dq^2 & 0 \\ -\sigma p & -1-q^2 \end{pmatrix}, \tag{19}$$

which has eigenvalues $\lambda_s(q) = -1-q^2$ and $\lambda_u(q) = p-\mu-Dq^2$. The eigenvalue λ_u can change of sign at $\mu_c = p$ and the equilibrium point changes its stability. The corresponding band of unstable modes is $\Delta q^2 = (p-\mu)/D$. thus, close to the instability of the bare soil solution $p = \mu$, slow spatial variations domain the dynamics ($\Delta q^2 \to 0$). We use a multiple time–space scale analysis to establish a simple normal form model Eq. (1). We choose a small parameter ϵ which measure the distance from the critical point $p = \mu$ as

$$p = \mu - \epsilon^2\eta, \tag{20}$$

then, $\Delta q^2 \sim \epsilon^2$. The non-trivial homogeneous equilibria read $w_1 = \mu/\left[(1-b)(1+\gamma b)^2\right]$ and $w_2 = p/\left[1+\sigma b(1+\gamma b)^2\right]$. The onset of bistability condition reads $\partial_b w_1|_{b=0} = \partial_b w_2|_{b=0}$, giving the critical relation $\sigma_c = 2\gamma - 1$. Thus, we perturb around this condition as

$$\sigma = 2\gamma - 1 - \epsilon\kappa. \tag{21}$$

To perform a weak nonlinear analysis, we consider the ansatz

$$\begin{pmatrix} b \\ w \end{pmatrix} = \begin{pmatrix} 0 \\ p \end{pmatrix} + \epsilon A(T,\mathbf{R})\vec{v}_1 + \epsilon^2\vec{W}^{[2]} + \epsilon^3\vec{W}^{[3]} + \cdots \tag{22}$$

where the slow time scale is $T = \epsilon^2 t$, and the space scale is $\mathbf{R} = \epsilon\mathbf{r}$. We insert the previous expressions for b and w, and expansions Eqs. (20), (21) in Eq. (18), and solve the linear problems for the unknown functions $\vec{W}^{[n]}$ corresponding to nonlinear corrections of order ϵ^n.

At order ϵ, one has

$$0 = \begin{pmatrix} 0 & 0 \\ -\sigma_c p & -1 \end{pmatrix} A\vec{v}_1, \tag{23}$$

which gives the eigenvector at instability

$$\vec{v}_1 = \begin{pmatrix} 1 \\ -\sigma_c p \end{pmatrix}. \tag{24}$$

At order ϵ^2, one finds

$$0 = \begin{pmatrix} 0 & 0 \\ -\sigma_c p & -1 \end{pmatrix}\vec{W}^{[2]} + A^2\begin{pmatrix} 0 \\ -\sigma_c p \end{pmatrix}, \tag{25}$$

which is solved for

$$\vec{W}^{[2]} = A^2\begin{pmatrix} 0 \\ -\sigma_c p \end{pmatrix}. \tag{26}$$

Finally, at order ϵ^3, we get the following linear inhomogeneous problem

$$\begin{aligned}\vec{v}_1\partial_T A = &\begin{pmatrix} 0 & 0 \\ -\sigma_c p & -1 \end{pmatrix}\vec{W}^{[3]} + A\begin{pmatrix} -\eta \\ 0 \end{pmatrix} + pA^2\begin{pmatrix} \kappa \\ 0 \end{pmatrix} + \\ &pA^3\begin{pmatrix} -3\gamma^2 \\ -\sigma_c(\gamma^2 - 2\gamma\sigma_c - \sigma_c) \end{pmatrix} + \nabla^2 A\begin{pmatrix} D \\ -\sigma_c p \end{pmatrix}.\end{aligned} \tag{27}$$

Introducing the inner product $\langle\vec{f}|\vec{g}\rangle \equiv \sum_i f_i g_i$, we search for the kernel of the adjoint of the linear operator acting on $\vec{W}^{[3]}$, which is

$$v^* = \begin{pmatrix} 1 \\ 0 \end{pmatrix}.$$

Then, for a linear problem of the form $Ax = b$, solutions exist whenever $\langle\ker(A^\dagger)|b\rangle = 0$. Applying the solvability condition to solve Eq. (27), we get

$$\partial_T A = -\eta A + p\kappa A^2 - 3\gamma^2 pA^3 + D\nabla^2 A. \tag{28}$$

By a renaming and scaling of variables and parameters, we recover the local FKPP Eq. (1).

References

[1] Lefever R, Lejeune O. On the origin of tiger bush. Bull Math Biol 1997;59(2):263–94.
[2] Lejeune O, Tlidi M. A model for the explanation of tiger bush vegetation stripes. J Veg Sci 1999;10:201–8.
[3] Macfadyen W. Vegetation patterns in the semi-desert plains of British somaliland. Geogr J 1950;116(4/6):199–211.
[4] Thiery J, d'Herbès J-M, Valentin C. A model simulating the genesis of banded vegetation patterns in Niger. J Ecol 1995;497–507.
[5] Klausmeier CA. Regular and irregular patterns in semiarid vegetation. Science 1999;284(5421):1826–8.
[6] HilleRisLambers R, Rietkerk M, van den Bosch F, Prins HH, de Kroon H. Vegetation pattern formation in semi-arid grazing systems. Ecology 2001;82(1):50–61.
[7] von Hardenberg J, Meron E, Shachak M, Zarmi Y. Diversity of vegetation patterns and desertification. Phys Rev Lett 2001;87(19):198101.
[8] Okayasu T, Aizawa Y. Systematic analysis of periodic vegetation patterns. Progr Theoret Phys 2001;106(4):705–20.
[9] D'Odorico P, Porporato A, Runyan CW. Dryland ecohydrology. Vol. 9. Springer; 2006.
[10] D'Odorico P, Laio F, Ridolfi L. Patterns as indicators of productivity enhancement by facilitation and competition in dryland vegetation. J Geophys Res Biogeosciences 2006;111(G3).
[11] Lejeune O, Tlidi M, Lefever R. Vegetation spots and stripes: dissipative structures in arid landscapes. Int J Quantum Chem 2004;98(2):261–71.
[12] Rietkerk M, Boerlijst MC, van Langevelde F, HilleRisLambers R, de Koppel Jv, Kumar L, et al. Self-organization of vegetation in arid ecosystems. Amer Nat 2002;160(4):524–30.
[13] Lejeune O, Tlidi M, Couteron P. Localized vegetation patches: a self-organized response to resource scarcity. Phys Rev E 2002;66(1):010901.
[14] Rietkerk M, Dekker SC, De Ruiter PC, van de Koppel J. Self-organized patchiness and catastrophic shifts in ecosystems. Science 2004;305(5692):1926–9.
[15] Vladimirov A, Lefever R, Tlidi M. Relative stability of multipeak localized patterns of cavity solitons. Phys Rev A 2011;84(4):043848.
[16] Fernandez-Oto C, Tlidi M, Escaff D, Clerc M. Strong interaction between plants induces circular barren patches: fairy circles. Phil Trans R Soc A 2014;372(2027):20140009.
[17] Clerc MG, Echeverría-Alar S, Tlidi M. Localised labyrinthine patterns in ecosystems. Sci Rep 2021;11(1):1–12.
[18] Berríos-Caro E, Clerc MG, Escaff D, Sandivari C, Tlidi M. On the repulsive interaction between localised vegetation patches in scarce environments. Sci Rep 2020;10(1):1–8.
[19] Tlidi M, Berríos-Caro E, Pinto-Ramo D, Vladimirov A, Clerc MG. Interaction between vegetation patches and gaps: A self-organized response to water scarcity. Physica D 2020;414:132708.
[20] Tlidi M, Lefever R, Vladimirov A. On vegetation clustering, localized bare soil spots and fairy circles. In: Dissipative solitons: from optics to biology and medicine. Springer; 2008, p. 1–22.
[21] Bordeu I, Clerc MG, Couteron P, Lefever R, Tlidi M. Self-replication of localized vegetation patches in scarce environments. Sci Rep 2016;6(1):1–11.
[22] Tlidi M, Bordeu I, Clerc MG, Escaff D. Extended patchy ecosystems may increase their total biomass through self-replication. Ecol Indic 2018;94:534–43.
[23] Tlidi M, Clerc M, Escaff D, Couteron P, Messaoudi M, Khaffou M, et al. Observation and modelling of vegetation spirals and arcs in isotropic environmental conditions: dissipative structures in arid landscapes. Phil Trans R Soc A 2018;376(2135):20180026.

[24] Domb C. Phase transitions and critical phenomena. Elsevier; 2000.
[25] Allen SM, Cahn JW. A microscopic theory for antiphase boundary motion and its application to antiphase domain coarsening. Acta Metall 1979;27(6):1085–95.
[26] Meron E. Pattern formation in excitable media. Phys Rep 1992;218(1):1–66.
[27] Flory PJ. Thermodynamics of high polymer solutions. J Chem Phys 1942;10(1):51–61.
[28] Bates FS. Polymer-polymer phase behavior. Science 1991;251(4996):898–905.
[29] Wang Z, Gao K, Kan Y, Zhang M, Qiu C, Zhu L, et al. The coupling and competition of crystallization and phase separation, correlating thermodynamics and kinetics in OPV morphology and performances. Nature Commun 2021;12(1):1–14.
[30] Tlidi M, Mandel P, Lefever R. Kinetics of localized pattern formation in optical systems. Phys Rev Lett 1998;81:979–82.
[31] Tlidi M, Mandel P, Le Berre M, Ressayre E, Tallet A, Di Menza L. Phase-separation dynamics of circular domain walls in the degenerate optical parametric oscillator. Opt Lett 2000;25(7):487–9.
[32] Tlidi M, Le Berre M, Ressayre E, Tallet A, Di Menza L. High-intensity localized structures in the degenerate optical parametric oscillator: comparison between the propagation and the mean-field models. Phys Rev A 2000;61(4):043806.
[33] Gomila D, Colet P, Oppo G-L, San Miguel M. Stable droplets and growth laws close to the modulational instability of a domain wall. Phys Rev Lett 2001;87(19):194101.
[34] Boeynaems S, Alberti S, Fawzi NL, Mittag T, Polymenidou M, Rousseau F, et al. Protein phase separation: a new phase in cell biology. Trends Cell Biol 2018;28(6):420–35.
[35] Lefever R, Turner JW. A quantitative theory of vegetation patterns based on plant structure and the non-local F–KPP equation. C R Méc 2012;340(11–12):818–28.
[36] Dornelas V, Colombo EH, López C, Hernández-García E, Anteneodo C. Landscape-induced spatial oscillations in population dynamics. Sci Rep 2021;11(1):1–11.
[37] Piva G, Colombo E, Anteneodo C. Interplay between scales in the nonlocal FKPP equation. Chaos Solitons Fractals 2021;153:111609.
[38] Fisher RA. The wave of advance of advantageous genes. Ann Eugen 1937;7(4):355–69.
[39] Kolmogorov AN. A study of the equation of diffusion with increase in the quantity of matter, and its application to a biological problem. Moscow Univ Bull Math 1937;1:1–25.
[40] Middleton N, Thomas D. World atlas of desertification. Arnold, Hodder Headline, PLC; 1997.
[41] Mauser W, Schädlich S. Modelling the spatial distribution of evapotranspiration on different scales using remote sensing data. J Hydrol 1998;212:250–67.
[42] De Gennes P-G, Prost J. The physics of liquid crystals. (83). Oxford University Press; 1993.
[43] Clavin P. Dynamic behavior of premixed flame fronts in laminar and turbulent flows. Prog Energy Combust Sci 1985;11(1):1–59.
[44] Coen S, Tlidi M, Emplit P, Haelterman M. Convection versus dispersion in optical bistability. Phys Rev Lett 1999;83:2328–31.
[45] Odent V, Tlidi M, Clerc MG, Glorieux P, Louvergneaux E. Experimental observation of front propagation in a negatively diffractive inhomogeneous Kerr cavity. Phys. Rev. A 2014;90:011806.
[46] Murray JD. Mathematical biology: I. an introduction. third ed.. New York, NY: Springer; 2002.
[47] Pismen LM. Patterns and interfaces in dissipative dynamics. Springer Science & Business Media; 2006.
[48] Strogatz SH. Nonlinear dynamics and chaos: with applications to physics, biology, chemistry, and engineering. CRC Press; 2018.
[49] Abràmoff MD, Magalhães PJ, Ram SJ. Image processing with ImageJ. Biophotonics Int 2004;11(7):36–42.
[50] Maestre FT, Escudero A. Is the patch size distribution of vegetation a suitable indicator of desertification processes? Ecology 2009;90(7):1729–35.
[51] Bak P. How nature works: the science of self-organized criticality. Springer Science & Business Media; 1996.
[52] Sornette D. Critical phenomena in natural sciences: chaos, fractals, selforganization and disorder: concepts and tools. Springer Science & Business Media; 2006.
[53] Clerc M, Falcon C, Tirapegui E. Additive noise induces front propagation. Phys Rev Lett 2005;94(14):148302.
[54] Braun OM, Kivshar YS. The Frenkel-Kontorova model: concepts, methods, and applications. Springer Science & Business Media; 2013.
[55] Pomeau Y. Front motion, metastability and subcritical bifurcations in hydrodynamics. Physica D 1986;23(1–3):3–11.
[56] Alfaro-Bittner K, Castillo-Pinto C, Clerc MG, González-Cortés G, Jara-Schulz G, Rojas RG. Front propagation steered by a high-wavenumber modulation: Theory and experiments. Chaos 2020;30(5):053138.
[57] Jara-Schulz G, Ferré MA, Falcón C, Clerc MG. Noise-induced kink propagation in shallow granular layers. Chaos Solitons Fractals 2020;134:109677.
[58] Meron E. Nonlinear physics of ecosystems. CRC Press Boca Raton, FL; 2015.